Density Reconstruction Using a Multi-Channel Far-Infrared Laser Interferometer and Particle Transport Study of a Pellet-Injected Plasma on the LHD

Kenji TANAKA, Kazuo KAWAHATA, Tokihiko TOKUZAWA, Shigeki OKAJIMA[1)], Yasuhiko ITO, Katsunori MURAOKA[1)], Ryuichi SAKAMOTO, Kiyomasa WATANABE, Tomohiro MORISAKI, Hiroshi YAMADA and the LHD Experimental group

National Institute for Fusion Science, Toki 509-5292, Japan
[1)]*School of Engineering, Chubu University, Kasugai 487-8501, Japan*

(Received 17 March 2008 / Accepted 16 June 2008)

Radial density profiles are obtained by applying the database slice and stuck density reconstruction technique to measured line-integrated densities, using multi-channel far-infrared laser interferometer installed on the Large Helical Device (LHD). A novel method that considers flux surfaces in the reconstruction process has been developed and applied successfully to a pellet-injected discharge in the LHD, enabling the identification of transient density peaking due to an inward pinch and enhanced diffusion in the edge region. The relationship between the change in particle transport and measured turbulence information obtained using reflectometry was also studied.

Keywords: multi-channel far-infrared interferometer, pellet injection, particle transport, convection velocity, diffusion coefficient, density peaking, Large Helical Device (LHD), reflectometry

DOI: 10.1585/pfr.3.050

1. Introduction

Radial electron density profiles are one of the most important physical quantities for the study of energy and particle transport of electrons and ions in magnetically confined plasmas. Several diagnostic methods such as multi-channel laser (or microwave) interferometry (MLI), laser Thomson scattering (LTS), microwave reflectometry, the lithium beam probe technique, and the polarimeter technique are available for the measurement of electron density profiles. Among these methods, the first two (MLI and LTS) are the most widely used in modern high-temperature plasma studies and are well developed and established. Also, these two methods have contrasting features for obtaining radial density profiles, i.e., MLI yields line-of-sight density profiles continuously in time, while LTS gives spatially resolved electron density and temperature profiles discretely in time. In addition, the detection of phases is sufficient for MLI, while elaborate absolute calibration of the detection optics is required for reliable measurements using LTS. For these reasons, MLI and LTS are complementary and both systems are often used in large plasma confinement experiments, sometimes more than one system of each method are used on a single machine.

The authors have attempted to exploit the potential of MLI for particle transport studies on the Large Helical Device (LHD) using a far-infrared (FIR) laser. For this purpose, a suitable process for the density reconstruction of line-of-sight signals from MLI is required for yielding reliable radial density profiles. In this article, a novel density reconstruction technique is described in which flux surfaces are considered appropriately, and its successful application using an FIR-MLI to the particle transport analysis of a pellet-injected plasma on the LHD is reported.

2. Density Reconstruction from a Multi-Channel Far-Infrared Laser Interferometer

The 13-channel FIR-MLI system was installed on the LHD [1], and it has been in routine operation since the second LHD experimental campaign in September 1998. The laser for the interferometer is a CO_2 laser pumped CH_3OH twin laser, having a wavelength of 119 μm. The details of the laser were described in Ref. [1] and references therein. An analog [2] and a digital [3] phase counters were used for phase detection. The resolutions of both phase counters were 1/100 fringes. The cross-sections of flux surface showing the beam path of FIR-MLI on the LHD at typical magnetic configurations are shown in Fig. 1. The chords of 13 channels cover the entire region of the plasmas. Figures 2 (a) and (b) show an example of measured line integrated densities using the FIR-MLI for a pellet injection discharge. Every chord successfully traced line-of-sight phase differences without fringe jump.

Many techniques [4–6] have been used to obtain density profiles from line-of-sight phase differences obtained

author's e-mail: ktanaka@nifs.ac.jp

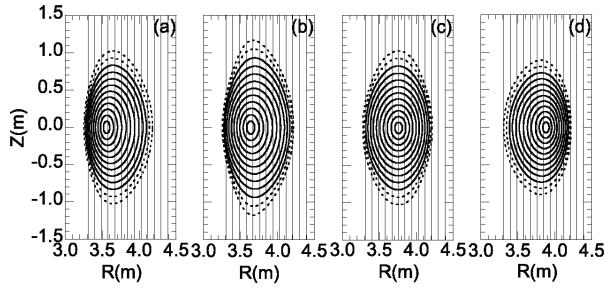

Fig. 1 Cross-section of flux surface showing the beam path of FIR laser interferometer. The beam axes are indicated by solid lines. The $1/e^2$ intensity full width is 42 mm. (a) The vacuum magnetic axis position (R_{ax}) = 3.5 m, (b) R_{ax} = 3.6 m, (c) R_{ax} = 3.75 m, and (d) R_{ax} = 3.9 m. Vacuum flux surfaces are shown for the step of ρ = 0.1 with solid lines (ρ = 0.1 - 1.0) and with dashed lines (ρ = 1.1, 1.2). ρ is the normalized averaged radius, as described in Sec. 2.2.

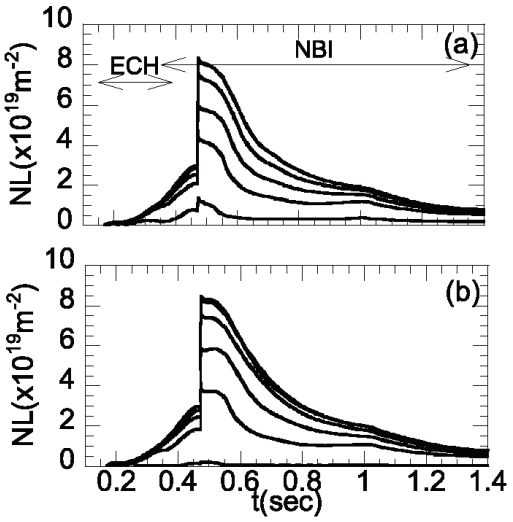

Fig. 2 Temporal evolution of line integrated densities measured using the 13-channel FIR interferometer. (a) From the lower to upper traces at R = 3.309, 3.399, 3.489, 3.579, and 3.669 m, (b) From upper to lower traces at R = 3.759, 3.849, 3.939, 4.029, 4.119, and 4.209 m. The plasma was produced using one 82.6 and two 84 GHz gyrotrons, and heated using two co- and counter-injected NBIs. The shot number was 6115. A pellet was injected at t = 0.47 sec. R_{ax} was 3.75 m, and the toroidal magnetic field at vacuum axis (B_t) was 1.5 T.

by performing MLI on non-circular plasmas. Since all these techniques were not applicable directly and/or were unsuitable for some reason for the present measurements on the LHD, the following novel technique has been developed.

The overall technique for standard density reconstruction is first described in Sec. 2.1. Then, we mention the points on which we paid special attention for its application to the analysis of transport in the LHD in Secs. 2.2 and 2.3. The overall algorithm of density reconstruction is shown in Sec. 2.4, and the error analysis is described in Sec. 2.5.

2.1 Database slice and stuck technique

The basic technique is the well-known slice and stuck technique (the onion peeling technique). In this method, flux surfaces are divided into several rings, and an averaged density is assigned to each ring. Then, line densities measured by MLI can be described by a linear combination of the line integrated density of each ring and can be expressed as follows:

$$\begin{aligned} NL_1 &= n_{e1}L_{11}. \\ NL_2 &= n_{e1}L_{21} + n_{e2}L_{22}. \\ NL_3 &= n_{e1}L_{31} + n_{e2}L_{32} + n_{e3}L_{33}. \\ &\cdot \\ &\cdot \\ NL_i &= n_{e1}L_{i1} + n_{e2}L_{i2} + n_{e3}L_{i3} + \cdot + n_{ej}L_{ij} + \cdot n_{ei}L_{ii}. \end{aligned} \quad (1)$$

where NL_i is the line integrated density of the i-th chord, n_{ei} is the averaged density of the i-th ring, and L_{ij} is the path length of the i-th chord in the j-th ring, as shown in Fig. 3. The n_{ei} can be obtained easily using a matrix inversion calculation, once all the line integrated densities NL_i are known. A reconstructed density profile consists of a discrete number of density histograms, as shown in the upper-right diagram of Fig. 3. To obtain good approximation of the histogram, the number of rings should be sufficiently large.

For the Abel inversion, the selection of an appropriate flux surface is essential. In the technique described in this article, an appropriate flux surface can be selected using interferometer data only from a pre-calculated equilibrium database. There is no need of supporting information from other measurements, such as magnetic measurements. However, the accuracy and validity of the measurements should be carefully examined, which were carried out in the present analysis.

To apply this technique to a specific measurement, the following items must be considered. First, how can we determine flux surfaces of a measured cross-section? Second, how can we determine the boundary condition? Third, how many rings are necessary? Fourth, how two reconstructions, namely, one from data outside the magnetic axis and the other inside it, can be compromised? Among these, the first item is the most important for density reconstruction on the LHD. Thus, it is treated extensively in Sec. 2.2, while the other items are briefly described in Sec. 2.3.

2.2 Determination of flux surfaces

Magnetic surfaces of the LHD are produced by external coils (helical, vertical, and local island diverter coils). Combinations of coil currents can vary features such as ellipticity, aspect ratio, magnetic shear, magnetic well, and

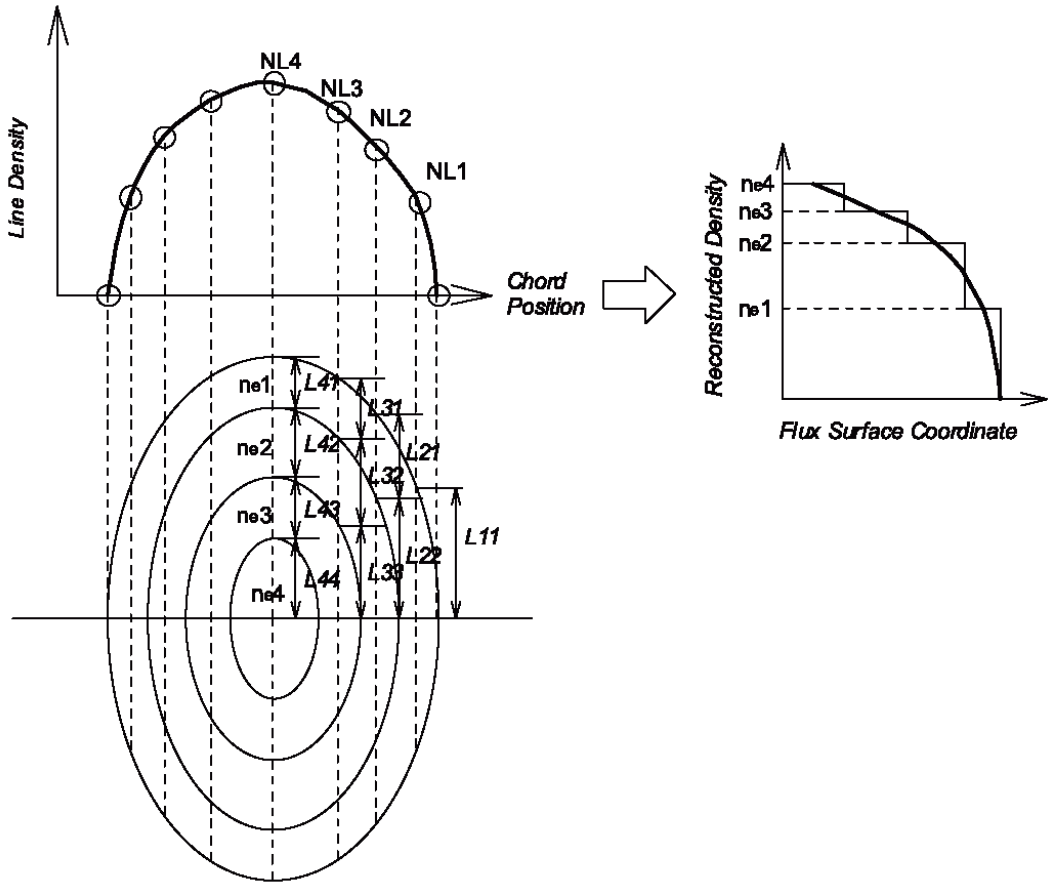

Fig. 3 Illustration showing the principle of the slice and stuck technique. For simplicity, only four rings are shown.

toroidal and poloidal ripples of magnetic structure. Transport characteristics and MHD stabilities depend on these features. As shown in Fig. 1, the shapes, sizes, and positions of magnetic axes are changed drastically by coil currents. Shifts in the axes change the flux surface shapes more sensitively in the core and less sensitively in the edge region. In addition, there is an effect of finite beta, which modifies these magnetic features. For density reconstruction, the shapes of magnetic surfaces and positions of magnetic axes are important parameters, which are decided by external coil currents, finite plasma pressures, and plasma currents, as described above.

For our database slice and stuck density reconstruction, several datasets of flux surfaces are prepared at different beta values for each configuration. For this purpose, 10 - 20 flux surface data for each configuration are calculated using the numerical MHD equilibrium code VMEC [7]. The VMEC calculation was performed by changing central beta values from 0% up to around 2% with steps of 0.1% or 0.2%. For this calculation, the following pressure profile was assumed:

$$p(\rho) = p(0)(1-\rho^2)(1-\rho^8), \qquad (2)$$

where the value of ρ is defined as the square root of the ratio of a toroidal flux inside a particular area to that bounded by the entire region inside the last closed flux surface (LCFS), which is defined in Sec. 2.3 (1). This profile well represents the datasets realized in the LHD. Even when the values of beta are low ($< \sim 2\%$), axis shifts are not negligible for determining the flux surface shapes, but pressure profiles are less sensitive. In other words, when beta values are low, the pressure at the plasma center is the dominant parameter for determining the position of axes and the shape of flux surfaces. Most LHD experiments have been performed at beta values lower than 2%, and the present database of flux surfaces, together with the assumption of Eq. (2) with different central beta values, can cover most flux surfaces realized in experiments. However, for higher beta values (of more than 2%), pressure profiles can significantly affect the shape of flux surfaces. In this case, the database should include other pressure profiles.

Both plasma pressure and current can induce magnetic axis shifts. In low-density plasmas ($< 2 \times 10^{19}\,\mathrm{m}^{-3}$), the tangentially injected neutral beam induces plasma current up to around 100 kA, and thus magnetic axis shifts. The VMEC calculation mentioned above does not include the plasma current explicitly. However, since both plasma pressures and currents induce vertical fields to cause magnetic axis shifts, we treated both these effects together, as represented by the effect of finite plasma pressures. In this

way, the best flux surface was selected from the set of the database using the scheme described in Sec. 2.4.

2.3 Other items

(1) Boundary condition

A plasma boundary, where densities become zero, is not well determined in helical devices, and this is a considerably different from the magnetic configurations of tokamaks. This is due to the presence of ergodic field traces at plasma edges. However, a plasma boundary has to be given externally for the VMEC calculation. Also, determination of a plasma boundary is necessary for density reconstruction.

The last closed flux surface (LCFS) is defined as a surface where the magnetic connection length becomes infinite. The magnetic connection length in the vacuum without any finite beta effects can be calculated by KMAG code [8]. KMAG code calculate the point, where connection length becomes infinite at divertor X point of horizontal elongated cross section. The flux surface passing through this position is defined as the LCFS. Line densities of interferometer chords passing around the LCFS are nonzero for most discharges. The electron temperature measured using LTS at LCFS is also not zero. This indicates that plasmas exist in the ergodic region.

Then, the question is how to determine the plasma boundary's position, where densities become zero. We have determined this position from the FIR-MLI measurements at the equatorial plane of the cross-section of FIR-MLI. As shown in Fig. 1, the FIR-MLI chords covered the larger major radius side of the plasma boundary region. The next question is how to determine the shape of the surface that passes through the zero density points. Strictly speaking, the existence of a closed surface outside of the LCFS is inconsistent with the existence of the ergodic region, where flux surfaces are not closed. However, the connection length close to the LCFS is of the order of several kilometers, while mean free path lengths of electrons at around the LCFS are of the order of several tens of meters. Thus, it is likely that electrons are not bound by the complicated structures of the ergodic region and we may assume that iso-density surfaces exist. Therefore, we added an additional surface using the result from the VMEC calculation for an expanded boundary condition. An example of the determination of such a boundary surface is shown below.

Since the chord number of the interferometer is limited, we adopted the following convention to determine the plasma boundary experimentally. Measured line density data were first fitted with a cubic spline curve, as shown in Fig. 4 (a). Then, the fitting curve was extrapolated to the zero crossing point at the larger radius side of the plasma boundary region. The value of ρ at the plasma boundary was determined from the interpolation between the LCFS and the expanded surface when the zero-density point existed between the two surfaces, or from the extrapolation from the expanded surface when the zero-density point did not exist between the flux surfaces. In the case of Fig. 4, the experimentally obtained zero density point at the larger major radius side of the plasma boundary is $R = 4.201$ m and corresponds to $\rho = 1.146$. The plasma boundary at the smaller major radius side of the plasma boundary is inaccessible by the FIR-MLI, as shown in Fig. 1. Therefore, the plasma boundary at this side was determined from that of the larger major radius side, as mentioned above and shown in Figs. 4 (a) and (b). However, at the inwardly shifted configurations of $R_{ax} < 3.6$ m, the boundary surface determined from the larger major radius side intersected with the vessel wall. For these cases, the wall position was used as the boundary position at the smaller major radius side.

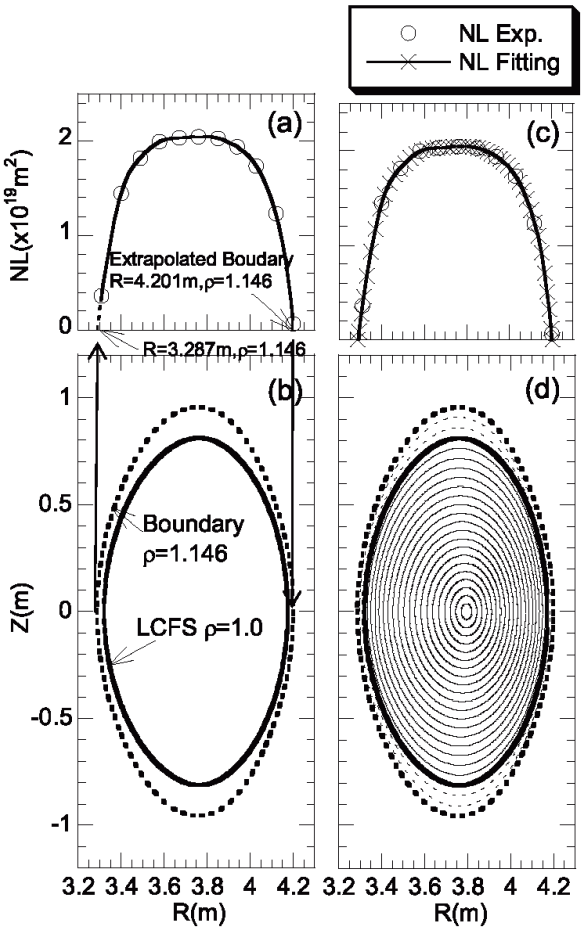

Fig. 4 (a), (c) Measured and fitted line density profiles, respectively, (b) Determination of the plasma boundary, (d) Rings for density reconstruction. Rings are from $\rho = 0.05$ to 1.146 with 0.05 step. The thick solid and dotted lines indicate the magnetic flux surface at $\rho = 1.0$ and plasma boundary. This is from LHD shot number 6115 at $t = 0.4$ s for $R_{ax} = 3.75$ m and $\beta(0) = 0.23\%$. The crosses in Fig. 4 (c) indicate interpolated and extrapolated line densities corresponding to the center of each ring.

(2) Number of rings

The number of rings for reconstruction should be sufficiently large to describe density profiles appropriately. Eleven FIR-MLI chords were used for the reconstruction shown in Fig. 4. If only these measured line density data were used for density reconstruction, the number of rings would become 5 or 6, which is very small to accurately describe the density profiles on the LHD. Thus, we followed the following convention.

Since the data points at these FIR-MLI chords were found to have very little noise contamination, we first fit a spline curve to best fit these data points. Presently, rings are separated at every $\rho = 0.05$ up to the plasma boundary (i.e., up to $\rho = 1.146$ in Fig. 4). Figure 4 (d) is one such example of ring separation, and Fig. 4 (c) shows the fitted data, where 45 fitted data for 23 rings were used for the reconstruction. The reconstructed data points are 23. This is a reasonable number to describe density profiles in the LHD, because the reconstructed profiles agreed well with YAG LTS, as described in Sec. 2.5.

2.4 Algorithm of density reconstruction

Figure 5 shows an algorithm of the database slice and stuck density reconstruction, using data for shot number 6115, which was performed with the vacuum magnetic axis positioned at $R_{ax} = 3.75$ m. Note that all the data shown in this article, including those in Sec. 3, are for this discharge. Figure 5 (a) illustrates that signals were obtained in 11 of 13 channels. The procedure described in Sec. 2.3 (2) is shown in Fig. 5 (e) at the time of 0.7 sec.

A set of databases of magnetic flux surfaces were constructed from the VMEC calculation assuming a pressure profile of Eq. (2). Flux surfaces were calculated from $\beta = 0\%$ to $\beta = 1.93\%$ with a step of 0.1% for this configuration, of which three examples are shown in Figs. 5 (b), (c), and (d) for beta values of 0, 0.69, and 1.93%, respectively. Each flux surface datum contains 32 surfaces; 31 of them are calculated inside the vacuum LCFS assuming a pressure profile of Eq. (2), while the remaining surface is added to define a plasma boundary, as described in Sec. 2.3 (1).

From the prepared flux surfaces at different beta values, such as those shown in Figs. 5 (b)-(d), we tentatively

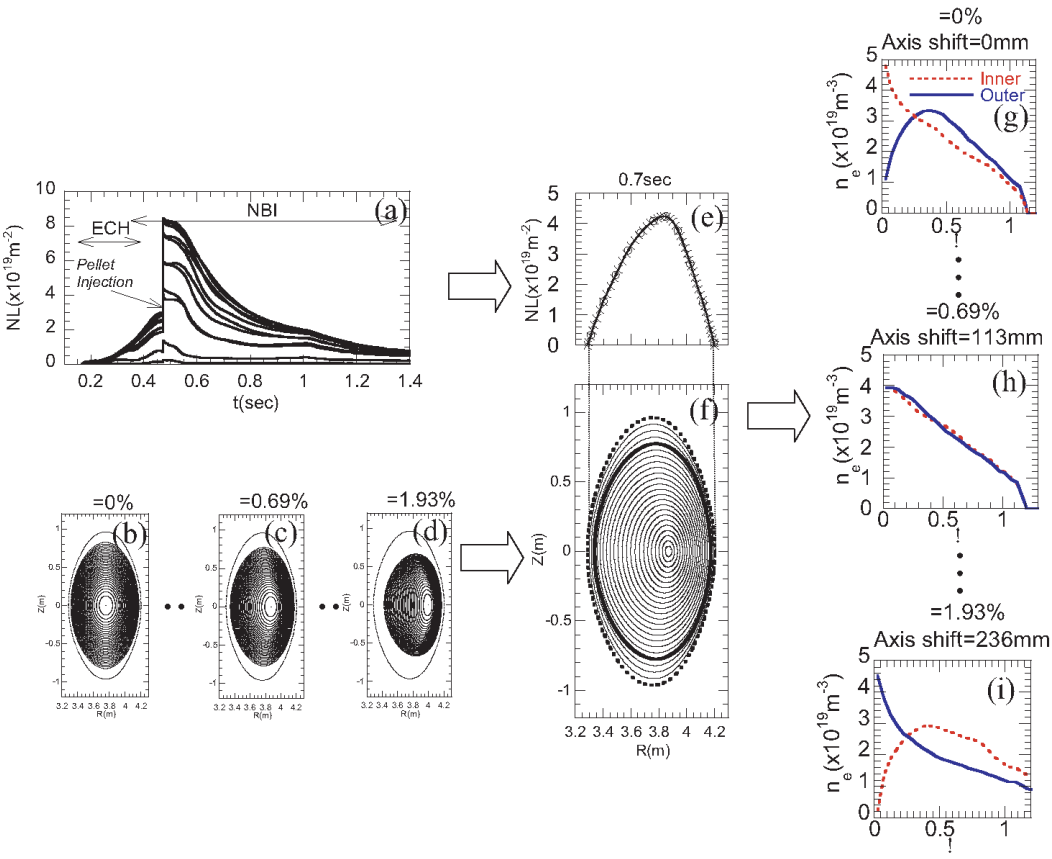

Fig. 5 Algorithm of density reconstruction. (a) Measured data of 11-channel line densities from LHD shot number 6115 for $R_{ax} = 3.75$ m. (b)-(d) Database of flux surfaces. (e) Spatial profile of the line density at $t = 0.7$ sec. Circles indicate experimental data and crosses indicate spline-fitted data. (f) Interpolated and extrapolated flux surfaces. The thick solid line indicates the last closed flux surface. An example of a flux surface for the beta value of 0.69% is shown. (g)-(i) Trials of density reconstruction using different flux data. Red dotted lines indicate profiles from the line integrated density data for reconstruction from the inner torus of the magnetic axis, while blue solid lines are from the outer torus of the magnetic axis.

selected one. Flux surfaces were interpolated or extrapolated from $\rho = 0.05$ towards both plasma boundaries with a step of $\rho = 0.05$. Then, the interpolated line integrated density data that correspond to the middle points of the respective rings were obtained. Finally, the local density in the rings between the surfaces was calculated from Eq. (1). These calculations were performed for different flux surfaces corresponding to different beta values. Since the density on the same flux surface should be the same, the best reconstructed density profile that yields the minimum difference in reconstruction profiles from the inner and outer magnetic axes is selected. Looking at Figs. 5 (g)-(i) from this viewpoint, it can be seen that the case where $\beta = 0.69\%$ (a magnetic axis shift of 113 mm) is the optimum.

Figure 6 shows an example of such density reconstruction for a pellet-injected shot (the same shot as Fig. 2, shot number 6115). The pellet was injected at $t = 0.47$ sec. The density increased rapidly after the pellet injection. In addition, line density profiles first changed from flat to peaked after the injection, and then went back from peaked to flat as shown in Figs. 6 (a)-(e). At each time, the density reconstruction procedures described above were followed. As shown in Figs. 6 (f)-(j), the reconstructed profiles obtained from data from the inner and the outer axes match reasonably well. Averaged profiles of inner and outer best-reconstructed profiles were used for the subsequent physics analysis. Figures 6 (k)-(o) shows the square difference of the inner and outer reconstruction at different beta, yielding different axis shifts. At each timing, square differences show a minimum value at a particular axis shift. This minimum is clearer at peaked density profiles, as shown in Figs. 6 (l)-(n), but it is not very clear at flat or hollow profiles, as shown in Figs. 6 (k) and (o). In this way, magnetic axis shifts were estimated only from FIR-MLI data. In Figs. 6 (a)-(e), the measured line integrated density was shown by a circle, and integrated line density of the reconstructed radial density, which was the averaged inner and outer reconstructed profile, was shown by crosses. They agree well, indicating that the reconstruction procedure was successful. Figure 7 shows the temporal evolution of radial density profiles in flux surface coordinates, determined from the above procedures. It is clear that the density profiles were hollow before pellet injection and became peaked after pellet injection.

2.5 Error sources of density reconstruction and validation with other diagnostics

Several error sources can distort reconstruction. Note that these sources should first be reduced by optimizing the procedures described above. Remaining residual errors

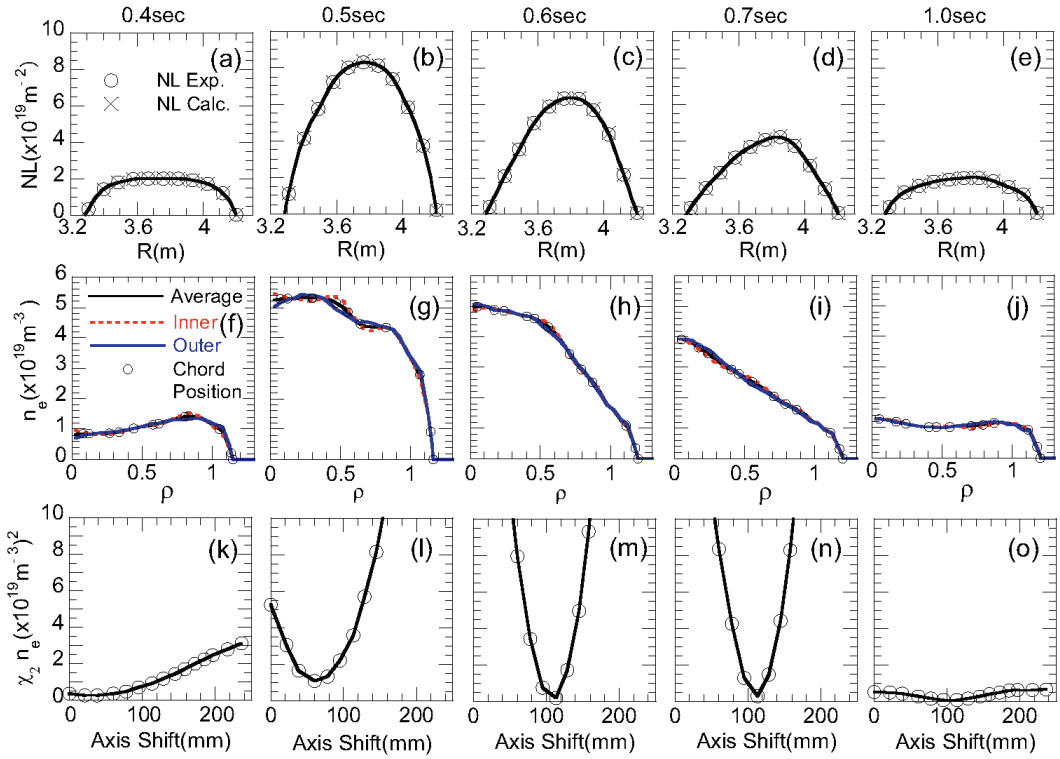

Fig. 6 Examples of density reconstruction. (a)-(e) Line integrated density profiles. Points of NL Exp. are measured line integrated density data, while those of NL Calc. are line integrated density data obtained from integration of reconstructed density profiles. Solid lines are fitted data with cubic spline used for density reconstruction. (f)-(j) Reconstructed radial density profiles. Normalized positions of the interferometer chords are shown with circles. Red dotted and blue solid lines indicate profiles from inner and outer wings of the magnetic axis. Black lines indicate averages of inner and outer profiles. (k)-(o) $\chi_2 n_e$ is the sum of the square of the difference of the reconstructed density between profiles from inner and outer axis data at each flux surface of the database.

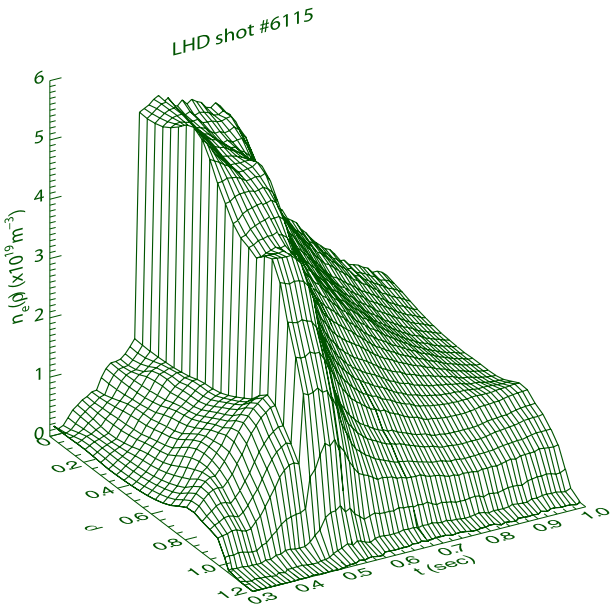

Fig. 7 Temporal change of electron density profiles in flux surface coordinates. Calculations were done every 10 msec.

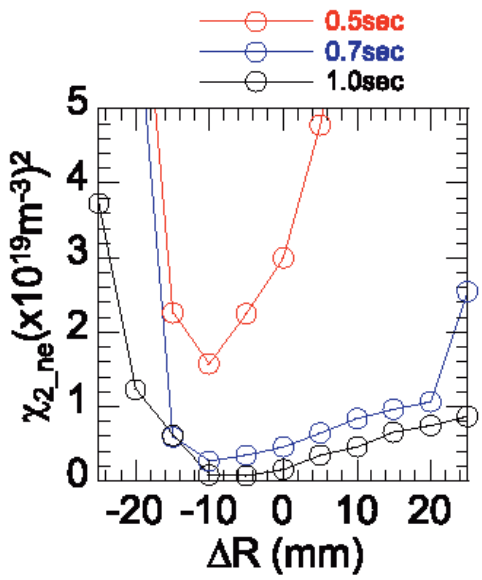

Fig. 8 Effects of the boundary chord's position at $R = 4.209$ m. Data at $t = 0.5$, 0.7, and 1.0 s of LHD shot number 6115 are examined. Negative and positive values of ΔR indicate inner and outer shift, respectively.

are to be estimated quantitatively and error bars of the reconstruction profiles shown. Comparisons with other measurements using different diagnostic techniques are also good for checking the accuracy of the present FIR-MLI measurement.

These errors may result from (i) the effects of mechanical vibrations, (ii) a finite beam width, (iii) beam positioning, (iv) a finite number of chords, and (v) the determination of the flux surface. These factors are discussed in turn below.

Regarding (i), all the detection optics were located in a vibration-protected stand, as shown in Ref. [1]. A small vibration remained with a frequency of around 100 Hz. However, its RMS amplitude was around 1% of one fringe, which corresponded to a line-averaged density of 3×10^{16} m^{-3} for a path length of 1.6 m. Most experiments were performed at densities above 1×10^{18} m^{-3}; therefore, the effect of mechanical vibration was negligible.

Regarding (ii), the beam width, which was defined as full width at the $1/e^2$ intensity of peaked intensity of a Gaussian laser beam, was 42 mm at a plasma, and it is reasonable to assume that the detector measured an average density within the beam width. We may assume that each detector was placed at the center of each beam, where the signal was the strongest. At the plasma edge, however, it is possible that the plasma density became zero within the beam. In this case, the center of the beam was no longer a representative position, as shown as the example in the magnetic configuration of data shown in Fig. 1 (c) for $R_{ax} = 3.75$ m. Therefore, the beam at $R = 4.209$ m was likely to cover the plasma boundary within the beam (42 mm width). To find a representative position, the position of the chord was scanned, and an optimum position was determined in such a way that the square difference between inner and outer reconstruction was minimized, as shown in Fig. 8. The position of the chord was scanned at ±25 mm from $R = 4.209$ m with a step of 5 mm. This test was performed for three cases at $t = 0.5$ s (a flat profile), 0.7 s (a peaked profile), and 1.0 s (a hollow profile). For these three cases, an inward shift by 10 mm was found to show the least square difference. Therefore, an inner shift by 10 mm ($R = 4.199$ m instead of $R = 4.209$ m) was used as a representative position.

Regarding (iii), the maximum beam shift due to refraction at 5×10^{19} m^{-3} was estimated to be around 5 mm. The accuracy of the beam positioning, which was estimated from measurements using a coaxial visible He-Ne laser, was less than 5 mm. Thus, the reconstruction procedures were repeated 100 times, assuming the beam positions to be distributed statistically, i.e., with a Gaussian distribution having a standard deviation of 5 mm. Then, we get 100 reconstructed profiles for the inner and outer magnetic axis each, i.e., 200 profiles in total. Figures 9 (a)-(c) show the reconstruction profiles with position errors; dotted lines indicate upper and lower error bars, which were defined as the standard deviation of 200 such profiles at each radial position. For the hollow (Fig. 9 (a)), flat (Fig. 9 (b)), and peaked (Fig. 9 (c)) profiles, estimated errors inside the LCFS were about ±6%.

Regarding (iv), although the number of chords was dictated by optical access to the LHD and other constraints, we wanted to know whether the present number (typically 11 channels) yielded sufficiently accurate electron density

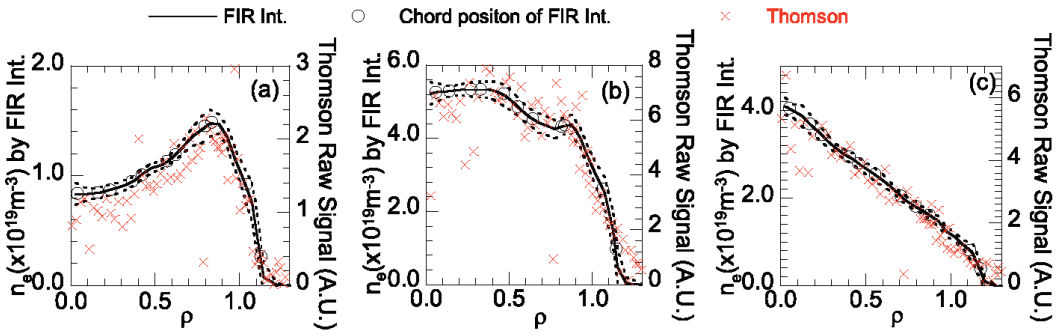

Fig. 9 Error estimates of density reconstruction assuming a position uncertainty of 5 mm and comparison with Thomson scattering signals at (a) $t = 0.4$ sec, (b) $t = 0.5$ sec, and (c) $t = 0.7$ sec. Normalized positions of the interferometer chords are shown with circles, and Thomson scattering data by crosses. Dotted lines are upper and lower ranges of densities from density reconstruction.

profiles. For this purpose, results from the present measurement were compared with those from an independent diagnostic for the same discharge. In Fig. 9, signal intensity profiles from YAG laser Thomson scattering (YAG-LTS [9]) are also shown. Because of technical difficulties with absolute calibration of Thomson signals, only raw signals are shown in Fig. 9. Since signal intensities are proportional to the electron density, comparisons of density profile shapes between the two diagnostics are possible. Figure 9 shows that the profile shapes from the two diagnostics, i.e., from hollow to peaked, agree reasonably well. However, note that signal intensities from YAG-LTS do not scale with those from reconstructed density profiles using FIR-MLI. For example, the central densities from FIR-MLI increased by a factor of 6.5 from $t = 0.5$ to $t = 0.7$ sec, while those from YAG-LTS changed by a factor of 5. Also, the central densities from FIR-MLI increased by a factor of 5 from $t = 0.5$ to $t = 1.0$ s, while YAG-LTS changed by a factor of 5.6. These differences were found to be caused by instability of the YAG laser pulses during an LHD discharge. After the fourth campaign (2000), the stability of the YAG laser was significantly improved, and the temporal changes in electron density data obtained from YAG-LTS have become much more reliable.

Considering all these effects, we conclude that the present 11 channels are reasonably good. However, when the number of working channels is reduced because of the fringe jump due to a strong density gradient, the quality of reconstruction profiles degrade.

Regarding (v), the accuracy of the determination of flux surfaces can be compared with that from other diagnostics. YAG-LTS determines flux surfaces from T_e profiles. The YAG-LTS system on the LHD measures electron density and temperature profiles along the major radius of the equatorial plane at the horizontally elongated cross-section [9]. Electron temperatures were measured in coordinates based on the major radius, $T_e(R)$, and they were converted to flux surface coordinate $T_e(\rho)$. By selecting an appropriate flux surface for FIR-MLI, as described in

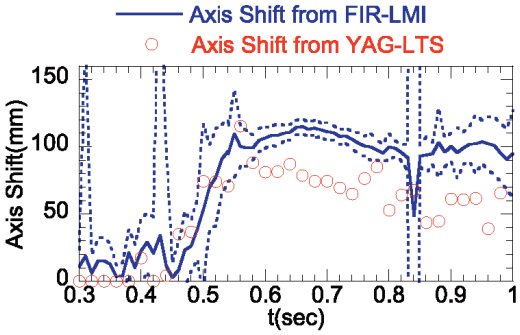

Fig. 10 Comparison of estimated positions of the magnetic axis from FIR-MLI and YAG-LTS. Dotted lines indicate upper and lower values due to the assumed random error of the chord position of 5 mm.

Sec. 2.4, flux surfaces for the coordinate conversion can be determined from the comparison of $T_e(\rho)$ by minimizing the difference from the inner to the outer magnetic axis. Electron temperature profiles from YAG-LTS are more accurate than electron density profiles, because the temperature measurement is much less sensitive to the calibration factor of the detectors. Therefore, electron temperature measurements were used to determine flux surfaces.

Figure 10 shows comparison of determination of flux surfaces between one using FIR-MLI and the other using YAG-LTS. In Fig. 10, the selected flux surface was indicated by the magnetic axis position depending on β. Since YAG-LTS and FIR-MLI are measured at the horizontally and vertically elongated cross-sections respectively, the magnetic axis shifts at vertically elongated cross-section are shown for comparison.

As shown in Fig. 10, the tendency of the time histories from both diagnostics is similar, but FIR-MLI shows more shifted values. As shown in Fig. 6, peaked density profiles measured using FIR-MLI show clear minima in the difference of inner and outer magnetic axis profiles, for

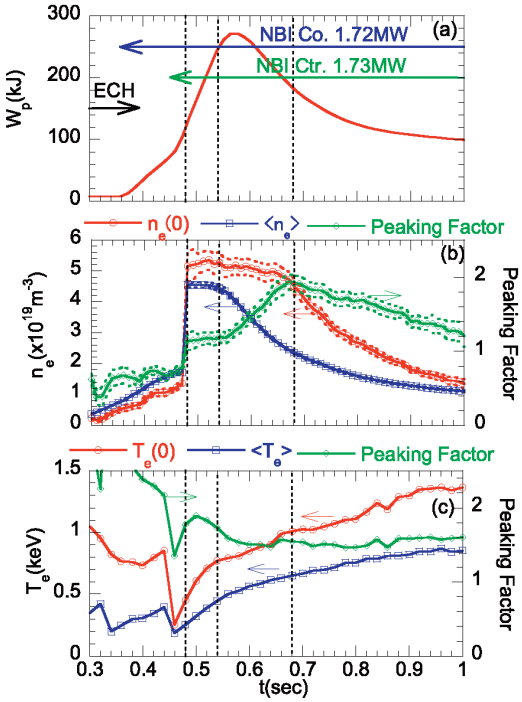

Fig. 11 Time histories of (a) the diamagnetic stored energy, (b) central and volume-averaged densities and the density peaking factor from FIR-MLI, and (c) central and volume-averaged temperatures and the temperature peaking factor from YAG-LTS. The peaking factor was defined as the ratio of central to volume-averaged values. Dashed lines in (b) indicate upper and lower ranges of each value due to the assumed random error of the chord position of 5 mm.

example, at t = 0.5 - 0.7 sec, but clear minima were not seen at hollow density profiles, such as those at t = 0.4 and 1.0 sec. Thus, peaked profiles can determine flux surfaces with better accuracy. Time histories of the peaking factor of $n_e(\rho)$ from FIR-MLI and that of $T_e(\rho)$ from YAG-LTS are shown in Figs. 11 (b) and (c), respectively. The peaking factor was defined as the ratio between the central and volume-averaged values. As shown in Fig. 11, $n_e(\rho)$ from FIR-MLI is more peaked than $T_e(\rho)$ from YAG-LTS at t = 0.6 - 0.87 sec. Thus, we conclude that FIR-MLI yields more accurate flux surfaces than YAG-LTS during this time period, while YAG-LTS yields better accuracy in other time periods. However, for more convenient analysis and superior time resolution of FIR-MLI (up to 10 μs) compared to YAG LTS (up to 20 ms), flux surfaces were all selected from FIR-MLI in the analysis in the following section.

3. Transport Analysis of a Pellet-Injected Discharge

As described in the previous section, FIR-MLI can provide temporal evolutions of electron density profiles in flux surface coordinates. Obtained data can be used for analysis of particle confinement of electrons. In particular, the ability to make temporally continuous density profile measurements offers several analysis schemes.

3.1 Analysis technique for particle transport from FIR-MLI data

The particle balance equation is expressed as follows:

$$\frac{\partial n_e}{\partial t} = -\nabla \cdot \Gamma + S = -\frac{1}{r}\frac{\partial}{\partial r} r\Gamma + S, \tag{3}$$

where n_e is the local electron density, Γ is the particle flux, and S is the local particle source rate. The particle flux is expressed as follows:

$$\Gamma = -D\nabla n_e + n_e V, \tag{4}$$

where D is the diffusion coefficient and V is the convection velocity. In Eq. (4), the first term is the particle flux driven by the density gradient, and the second term is the convection flux, which is driven by other gradients such as an electron temperature gradient, an ion temperature gradient, a potential gradient, or a momentum gradient. The convection flux represents all these effects together, excluding the density diffusive flux. Peaked density profiles in a tokamak and hollowed density profiles in a heliotron/stellarator in steady equilibrium states were frequently observed, and these observations can be explained only by the existence of the convection flux. However, simple particle balance cannot discriminate D from V, and additional information such as the temporal development of density profiles is necessary to distinguish them.

One approach is to perturb electron densities by a periodic change of gas fueling, and to estimate D and V from the propagation of modulation [10–12]. Another approach is to estimate D and V from temporal changes of the flux and gradient [13, 14]. The local particle flux can be estimated from temporal changes of the local density and particle source, as shown in Eq. (3), together with Eq. (4). The relationship between the density gradient and the particle flux, both being normalized by the local density, yields the diffusion coefficient and the convection velocity, as shown by the following equations:

$$\frac{\Gamma}{n_e} = -D\frac{\nabla n_e}{n_e} + V, \tag{5}$$

$$\Gamma(r) = \frac{1}{r}\int_0^r r\left(S - \frac{\partial n_e}{\partial t}\right)\mathrm{d}r. \tag{6}$$

Equation (5) indicates that the plot of the left-hand side against the first term of the right-hand side (the density gradient portion) gives D as a coefficient and V as an offset value. This analysis was previously performed by observing the effects of the periodic modulation of gas fueling in Joint European Torus (JET) [13] and of temporal change of gas fueling in Compact Helical System (CHS) [14]. The difficulty of this analysis lies in the estimation of the particle source rate S. The particle source rate from the neutral

beam injection (NBI) can be estimated from the numerical code with a known input beam power, and plasma density and temperature profiles. On the other hand, the particle source rate from gas fueling and wall recycling are difficult to estimate from experimental observations, because neutrals that produce electrons are highly asymmetric in vacuum vessels. In Ref. [13], the absolute value of S was determined from the penetration of the modulation. In Ref. [14], hydrogen atom densities were measured using laser-induced florescence spectroscopy (LIFS), and S was estimated from a combination of results from LIFS and a 3-D Monte Carlo simulation.

However, when S is negligibly small compared with the time derivative of a local density, one sees from the bracket in the integral of Eq. (6) that it does not affect the particle flux. In fact, 3-D Monte Carlo simulation in the LHD [11, 12, 15] showed that the peak of S was around $\rho = 1.1$ and decreased by one order of magnitude at $\rho = 1.0$ when the electron density was around $1.5 \times 10^{19}\,\mathrm{m}^{-3}$ and the electron temperature around 250 eV. Therefore, it is reasonable to neglect S when considering gas fueling and wall recycling inside of around $\rho = 1.0$, namely, inside the LCFS. This assumption is more appropriate when the time derivative of the density is large, which is the case after pellet injection.

Summing up the above arguments, we consider only S from NBI and neglected the contribution of S from wall recycling and gas puffing, and the particle source from NBI was estimated using FIT code [16].

3.2 Characteristics of particle confinement after pellet injection

Figure 11 shows temporal changes in (a) the diamagnetically measured stored energy, central and volume-averaged values, and peaking factor of (b) electron density and (c) electron temperature. The magnetic axis was at $R_{ax} = 3.75$ m with $B_t = 1.5$ T, and the working gas was hydrogen. The plasma was first pre-ionized using a gyrotron operating at 82.7 and 84 GHz (second harmonic resonant heating), and then co- and counter-directed tangential NBI were injected. An ice pellet [17] was injected after the NBI injection. The central density and temperature were values at the plasma center ($\rho = 0$). The volume-averaged density was calculated within the LCFS. The peaking factor was defined as a central value divided by a volume-averaged value.

In Fig. 11, three vertical dotted lines are indicated, which show times when particle transport markedly changed as shown below. The first is at $t = 0.48$ sec, just after an ice pellet was injected. The second is at $t = 0.54$ sec, when the volume-averaged density started to decrease, and the density peaking factor started to increase. The third is at $t = 0.68$ sec, when the peaking factor reached a maximum.

As shown in Fig. 11, just after a pellet was injected at $t = 0.48$ sec, the density profile became peaked, and central and volume-averaged values stayed constant until around $t = 0.54$ sec. Figure 12 shows the temporal evolution of density and temperature profiles. Density profiles changed from hollow to peaked, as shown in Fig. 12 (a), after the pellet injection, and the central electron temperature decreased from 0.85 keV to 0.45 keV, as shown in Fig. 12 (b). As shown in Fig. 11 (b), central and volume-averaged densities started to decrease at around $t = 0.54$ sec; i.e., the central density decreased slowly and the volume-averaged density more rapidly after $t = 0.54$ sec, implying that density profiles became peaked again after this time. Density peaking factors increased until $t = 0.68$ sec. Therefore, we refer to the time interval of $t = 0.54$ - 0.68 s as the "*additional density peaking phase*." As shown in Fig. 12 (c), during this phase, the density gradient became very steep at $\rho < 0.9$.

As shown in Fig. 11 (b), the central density started to decrease more rapidly than the volume-averaged value after $t = 0.68$ sec, implying that the density peaking factor started to decrease. Thus, we call the time interval of $t = 0.68$ - 1.0 sec as the "*density broadening phase*." As shown in Fig. 12 (c), although the densities at $\rho < 0.9$ were reduced, the edge densities at $\rho > 0.9$ were almost constant.

The stepwise changes of density profiles shown in Figs. 11 (b) and 12 (a) and (c) suggest that particle transport may have experienced a transition from one phase to another. On the other hand, both central and volume-

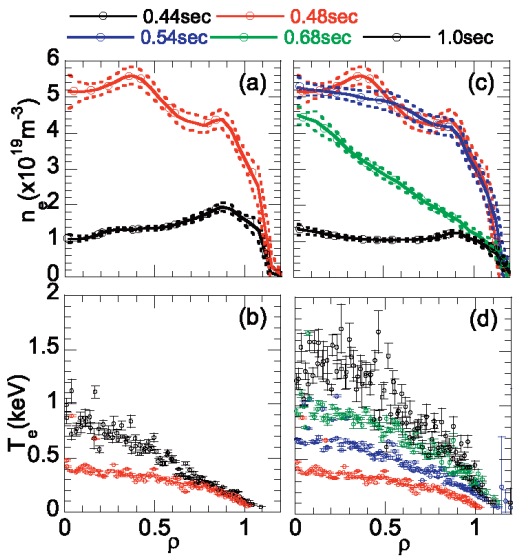

Fig. 12 (a) Density and (b) temperature profiles just before ($t = 0.44$ sec) and just after ($t = 0.48$ sec) pellet injection; (c) and (d) are the respective profiles for the density decay phase after pellet injection at $t = 0.48$, 0.54, 0.68, and 1.0 s. Dashed lines indicate upper and lower ranges of each value in (a) and (c) due to the assumed random error of the chord position of 5 mm.

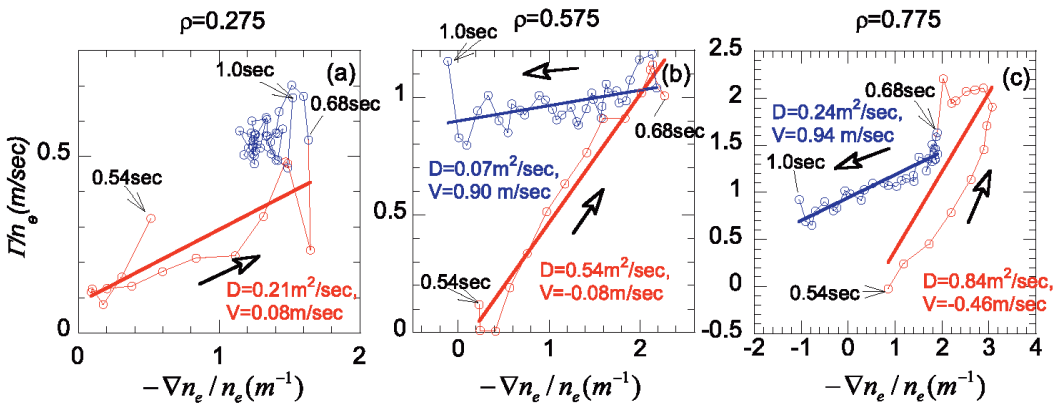

Fig. 13 Relationship between the normalized density gradient $-\nabla n_e/n_e$ and the normalized particle flux Γ/n_e at (a) $\rho = 0.275$, (b) $\rho = 0.575$, and (c) $\rho = 0.775$. The values are averages of 100 times error analysis assuming random error of the chord position of 5 mm.

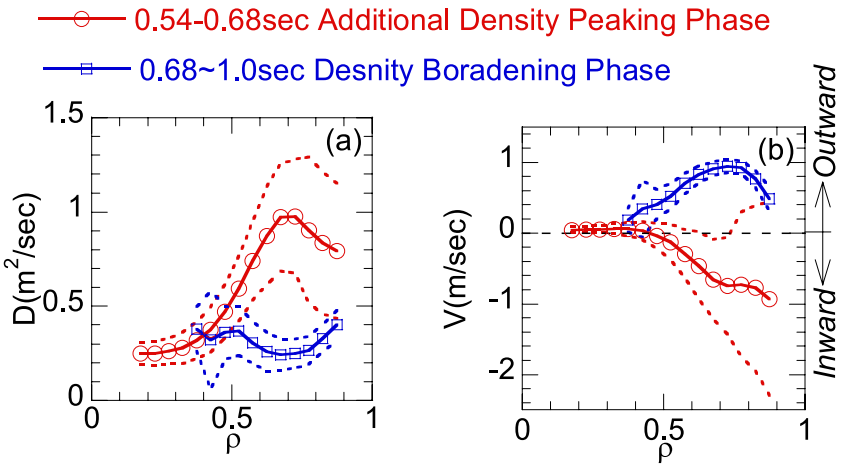

Fig. 14 Changes in spatial profiles of (a) the diffusion coefficient and (b) the convection velocity during the additional density peaking phase (t = 0.54 - 0.68 sec) and the density broadening phase (t = 0.68 - 1.0 sec). Dashed lines indicate upper and lower ranges of estimated errors.

averaged electron temperatures increased similarly after t = 0.54 sec, implying that the peaking factor of $T_e(\rho)$ was almost constant and did not show any stepwise change of profiles, as shown in Figs. 11 (c) and 12 (d).

Two different phases in density profiles after pellet injection, the additional density peaking phase at t = 0.54 - 0.68 sec, when the peaking factor increased, and the density broadening phase at t = 0.68 - 1.0 sec, when the peaking factor decreased, were analyzed using a plot of normalized flux (Γ/n_e) against normalized density gradient ($-\nabla n_e/n_e$), as discussed in Sec. 3.1.

Figure 13 shows such plots for three radial positions, ρ = 0.275, 0.575, and 0.775, from t = 0.54 to 1.0 sec. These analyses were carried out 100 times by assuming random errors of 5 mm in laser positions, as discussed in Sec. 2.5. Values shown in the abscissas and ordinates are averages of these 100 trials at each time. Two different slopes are apparent at ρ = 0.575 (Fig. 13 (b)) and ρ = 0.775 (Fig. 13 (c)). In contrast, we see only one slope at t = 0.54 - 0.68 s at ρ = 0.275 (Fig. 13 (a)), since the normalized density gradient did not change dramatically after t = 0.68 sec. The two slopes in Figs. 13 (b) and (c) indicate that two different phases of transport, and specifically a transition between them, exist, which was already suggested from the change of density profile peaking factors described above. The slope in this plot of $-\nabla n_e/n_e$ vs Γ/n_e at ρ = 0.575 clearly changed at t = 0.68 sec as shown in Fig. 13 (b). This time corresponds to the third vertical dotted line in Fig. 11, where the peaking factor reached a maximum value.

D and V were evaluated from Figs. 13 (a)-(c) following the procedure described in Sec. 3.1 for the additional density peaking phase (t = 0.54 - 0.68 sec) and the density broadening phase (t = 0.68 - 1.0 sec). Figure 14 shows the values of D and V for these two phases. Solid lines indicate averages, and dashed lines show the upper and lower bounds of error bars, which are defined as standard deviations of estimation. We reiterate that the density profile's

temporal history data consisted of 100 data sets, which were obtained from error analysis with 100 times instances random position error analysis. The determination of D and V from the slope was carried out for each of the 100 data sets for the temporal evolution of the density profile. The slope was not well defined at $\rho < 0.175$ for the additional density peaking phase and at $\rho < 0.375$ for the density broadening phase ($0.68 < t < 1.0$ sec). The data at $\rho > 0.875$ were excluded because particle sources from wall recycling and gas puffing, which were not taken into account here, can affect particle transport. The estimated D and V are from the least square fitting of the slopes, where correlation coefficients of fitting were larger than 0.4.

As shown in Fig. 14, during the additional density peaking phase, diffusion coefficients increased toward the edge. The convection velocities were negative (inward directed) and its absolute values increased toward the edge. During the density broadening phase, the diffusion coefficients were more or less spatially constant. The convection velocities were positive (outward directed) and showed a maximum value at $\rho = 0.725$.

We note that in the equilibrium steady state, the same magnetic configuration ($R_{ax} = 3.75$ m, $B_t = 1.5$ T) yielded hollow density profiles, similar to the one for $t = 0.44$ sec of Fig. 12 (a). The estimated D and V for the density broadening phase ($t = 0.68$ - 1.0 sec) were similar to those obtained from density modulation experiments at similar densities and temperatures [12]. These results suggest that particle transport during the density broadening phase shows similar characteristic of conventional gas puffing discharges, which was reported in Refs. [12, 18], and [19]. In conventional discharges at $R_{ax} = 3.75$ m with gas puffing, the density peaking factor was reduced with decreasing collisionality [18, 19]. The hollow density profiles were explained by the neoclassical outward convection [12]. Therefore, in the density broadening phase ($t = 0.68$ - 1.0 sec), the reduced peaking factors and resultant density profile change from peaked to hollow can be well explained by the increase of neoclassical outward convection with decreasing collisionality [12].

On the other hand, transport for the additional density peaking phase ($t = 0.54$ - 0.68 sec) is observable only after pellet injection, and the transport characteristics cannot be explained by the role of neoclassical transport, which is different from that for the density broadening phase ($t = 0.68$ - 1.0 sec). Namely, during the additional density peaking phase, the density peaking factor increased with increasing temperature (i.e., with decreasing collisionality). This increase in peaking was achieved by enhanced diffusion at $\rho > 0.5$ associated with an inwardly directed pinch, the existence of which is clear because normalized particle fluxes (Γ/n_e) are extrapolated to negative values when normalized density gradients ($-\nabla n_e/n_e$) are zero (cf. Eq. (5)) at $\rho = 0.575$ and $\rho = 0.775$ as shown in Figs. 13 (b) and (c). This fact is also evidenced in Fig. 14 (b).

3.3 Response of turbulent fluctuations in the two different transport phases

An inwardly directed pinch in the heliotron configuration cannot be explained by the neoclassical theory, as

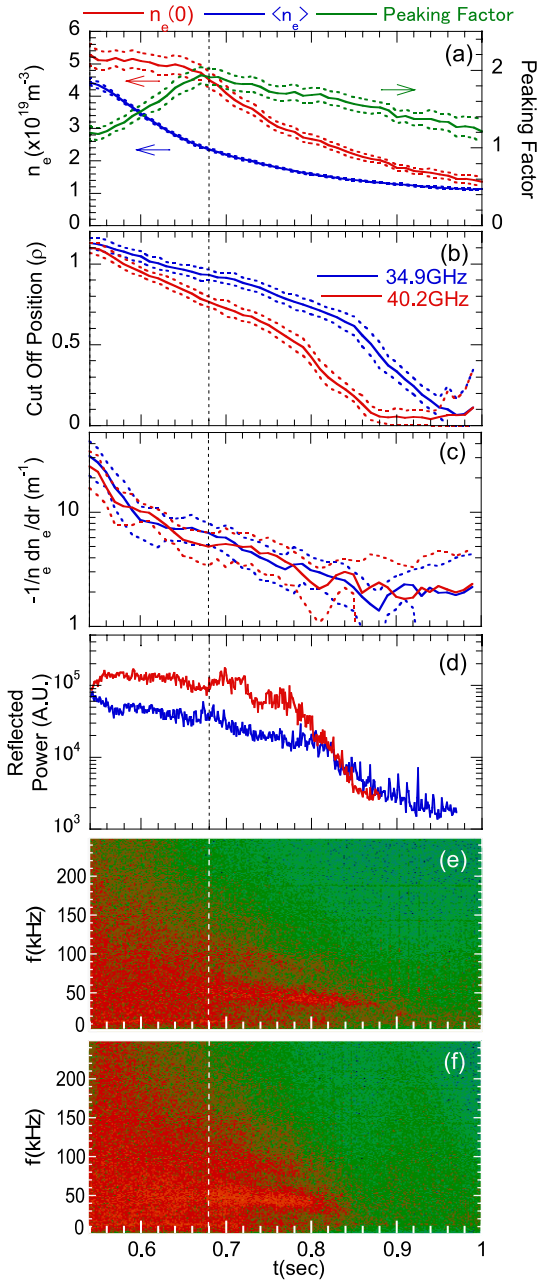

Fig. 15 Time trace of (a) central and volume-averaged density, and density peaking factor, (b) cut-off layer position of reflectometer, (c) $-\nabla n_e/n_e$ at cut-off position, (d) reflected power, (e) power spectrum of 34.9 GHz O mode reflectometer, (f) power spectrum of 40.2 GHz O mode reflectometer. The traces of additional peaking ($t = 0.54$ - 0.68 sec) and broadening ($t = 0.68$ - 1.0 sec) phases are shown. Dotted line is at $t = 0.68$ s, the moment of transition from the additional density peaking to the density broadening phase. Reflectometer signals were filtered above 10 kHz. The sampling time was 500 kHz. In (e) and (f), red and green indicate stronger and weaker power, respectively.

described above. Recently, it has been reported that drift-wave-like turbulence, such as the ion temperature gradient mode and trapped electron mode, can induce peaked density profiles in tokamaks [20]. In addition, such turbulence may have also induced an inwardly directed flux in the LHD [21]. The response of turbulent fluctuations in the additional density peaking and density broadening phases was studied using a microwave homodyne reflectometer. The reflectometer was originally constructed for the NBI interlock as a simple density monitor [22]. The microwave sources' frequencies were 34.9 GHz and 40.2 GHz, and the injection was in an O mode. Therefore, the cut-off densities were 1.5×10^{19} m^{-3} and 2×10^{19} m^{-3}, respectively. For signal detection, a simple homodyne system was used. Although the signals are rough indicators of fluctuation powers at cut-off layers, interpreting them is not straightforward. A comparison of intensities between the two frequencies is not possible, because the signals were neither absolutely nor relatively calibrated. Also, the measured positions (the positions of cut-off layers) change with time. Care must therefore be taken in interpreting the obtained homodyne reflectometer signals.

Figure 15 shows time traces of the density profile parameter, cut-off position, and spectrum behavior during the additional density peaking (t = 0.54 - 0.68 sec) and broadening (t = 0.68 - 1.0 sec) phases. As densities decrease, cut-off layers move inward, as shown in Fig. 15 (b). The normalized density gradient $-\nabla n_e/n_e$ at cut-off layer positions decreased in time, as shown in Fig. 15 (c). Reflected power also decreased, as shown in Fig. 15 (d). This is qualitatively consistent with the mixing length estimate, which yields fluctuation levels proportional to the normalized density gradient for a given fluctuation wavenumber [23].

The temporal information for the cut-off layers (Fig. 15 (b)) is combined with that of reflected power (Fig. 15 (d)) to yield spatial distributions of the latter quantity, as shown in Fig. 16. From this figure, one sees that the reflected power increases towards the plasma edge, suggesting that turbulence intensities also increase in that direction. This is qualitatively consistent with observations in toroidal devices [23].

Figures 15 (e) and (f) indicates temporal changes in the frequency power spectra, where broad-band frequency features are observed. Although a reflectometer cannot determine the wavenumbers of turbulence, observed features

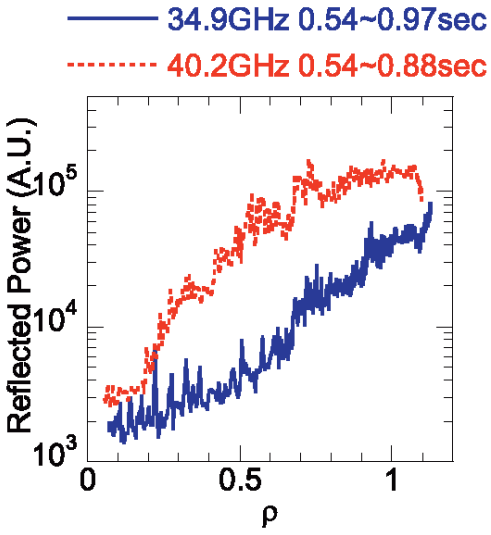

Fig. 16 Spatial profiles of reflected power obtained from Figs. 15 (b) and (d). The signals are from the time when cut-off layer positions were at $\rho > 0.05$.

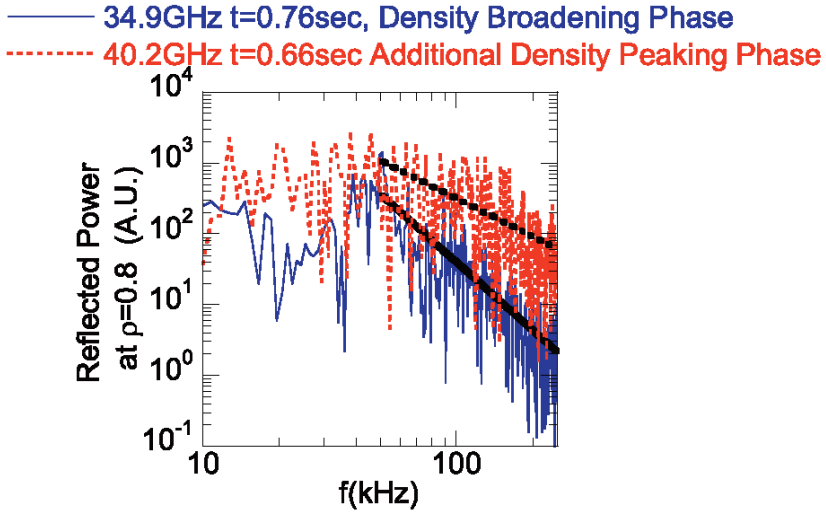

Fig. 17 Comparison of frequency power spectrum at $\rho = 0.8$ between the additional density peaking phase from the 40.2 GHz signal and the density broadening phase from the 34.9 GHz signal. Thick black lines indicate the exponential fitting for components higher than 50 kHz. The exponents of 34.9 GHz and 40.2 GHz are −3.2 and −2.2, respectively.

of broad-frequency spectra are similar to those measured using phase contrast imaging [11, 12]. A possible candidate for turbulence is drift-wave type turbulence, such as the ion temperature gradient mode or trapped electron mode. Wavenumbers for these modes are expected to be around $k\rho_i$ = 0.1 - 1 [21, 24], where k is the perpendicular wavenumber and ρ_i is the ion Larmor radius.

As described in the previous section, a clear difference in transport characteristics is observed between the additional density peaking (t = 0.54 - 0.68 sec) and density broadening (t = 0.68 - 1.0 sec) phases. If turbulence causes such a difference, a clear difference in turbulence characteristics should also be observed. To observe this experimentally, reflectometer power spectra were compared at the two different transport phases at a single location. As seen from Fig. 15 (b), this was possible only in a small window of around ρ = 0.8, since cut-off layer positions change with time. Thus, signals at t = 0.66 sec for 40.2 GHz for the additional density peaking phase and at t = 0.76 sec of 34.9 GHz for the density broadening phase were selected to compare fluctuation spectra at ρ = 0.8. Figure 17 shows these spectra. The shapes of the observed frequency spectra were fitted to the following equation in frequency regimes higher than 50 kHz, and frequency exponents were obtained,

$$S(f) \propto f^{\text{exponent}} \tag{7}$$

Figure 17 shows that the exponents are −2.2 and −3.2 in the additional density peaking and broadening phases, respectively, showing that a broader frequency power spectrum was observed at the former phase. This may account for the observed larger diffusion coefficient and inward convection velocity for the former phase, as shown in Figs. 14 (a) and (b) at ρ = 0.8.

4. Discussion and Summary

Density profiles in flux surface coordinates were obtained using only FIR-MLI data. For this purpose, a novel reconstruction technique has been developed that takes into account non-circular cross-sections of flux surfaces using the numerical equilibrium code VMEC for central beta values from 0% to 2%. The method also includes proper considerations for the number of rings and for reconciling the outer and inner reconstructions of the vertical minor cross-sections of the LHD, where the FIR-MLI data were obtained. The usefulness of this reconstruction scheme has been vividly demonstrated in the particle transport analysis of a pellet-injected discharge in the LHD, where the diffusion coefficient and convection velocity were obtained for the additional density peaking phase and the density broadening phase of the discharge. In particular, we stress the importance of the finding of an inwardly directed pinch, which contributed to peaked density profiles in the additional density peaking phase. This inwardly directed pinch may have been induced by turbulence-driven anomalous transport, similar to that observed in some tokamaks. The observed fluctuation signals from a microwave reflectometer qualitatively support this.

The reconstruction procedure, described in detail in Sec. 2, requires a constant density on a flux surface and poloidal symmetry. When poloidal symmetry is violated, for example, due to the existence of magnetic islands, another technique was attempted [25], where a procedure for fitting an analytical expression of the density profiles was combined with information about the island structure. An alternative is to determine flux surfaces from the iteration of the equilibrium calculation, and this calculation was carried out using the TOTAL code [26]. For this purpose, the assumption of equal ion and electron temperatures, together with self-consistently determined electron density profiles, allowed the equilibrium to be reconstructed. The results thus obtained were compared with those from the method described here, and they nearly agreed. However, when the plasma current is not negligible (for example, when the beam driven current is significant), the TOTAL code failed to produce an appropriate flux surface coordinate.

One of the limitations of FIR-MLI is caused by refraction of laser light at high density ($>10^{20}$ m^{-3}), resulting in loss of heterodyne beating signals. The edge channel started to lose signals because of the existence of a high density gradient, decreasing the measurement accuracy of density profiles. Recently, a CO_2 laser imaging interferometer (CO_2-LII) was constructed [27–29]. The CO_2-LII works at extremely high densities of up to 1×10^{21} m^{-3}, but compensation for mechanical vibration is necessary. If vibration compensation is not perfect, signals include noise due to uncompensated vibration, resulting in line density profiles that are not smoothly connected. In this case, the technique described in Sec. 3 is inadequate, and another method [29] was tried, the least square technique combined with spatial regularization.

Recently, the super dense core (SDC) shot was obtained [30], which suggests improvements of core particle confinement, and the SDC has given great impact to the realization of a high density reactor scenario. Analysis similar to that shown in Sec. 3 was carried out using the CO_2-LII and reported in Ref. [31].

[1] K. Kawahata, K. Tanaka, Y. Ito, A. Ejiri and S. Okajima, Rev. Sci. Instrum. **70**, 707 (1999).

[2] Y. Ito, K. Haba, T. Tokuzawa and K. Kawahata, Fusion Eng. Des. **56-57**, 965 (2001).

[3] T. Tokuzawa, K. Kawahata, K.Tanaka, Y. Ito, A. Ejiri and T. Simizu, Rev. Sci. Instrum. **72**, 1103 (2001).

[4] H.K. Park, Plasma Phys. Control. Fusion **31**, 2035 (1989).

[5] J.P.T. Koponen and O. Dumbrajs, Rev. Sci. Instrum. **68**, 4038 (1997).

[6] I. Furuno *et al.*, Plasma Phys. Control. Fusion **47**, 46 (2005).

[7] S.P. Hirshman and J.C. Whitson, Phys. Fluids **26**, 3553 (1983).

[8] T. Morisaki *et al.*, J. Nucl. Mater. **313-316**, 548-552 (2003).
[9] K. Narihara *et al.*, Rev. Sci. Instrum. **72**, 1122 (2001).
[10] K.W. Gentle *et al.*, Plasma Phys. Control. Fusion **29**, 1077 (1987).
[11] K. Tanaka *et al.*, Nucl. Fusion **46**, 110 (2006).
[12] K. Tanaka *et al.*, Fusion Sci. Tech. **51**, 97 (2007).
[13] J. O'Rourke *et al.*, Plasma Phys. Control. Fusion **35**, 585 (1993).
[14] H. Takenaga *et al.*, Nucl. Fusion **35**, 107 (1995).
[15] M. Shoji *et al.*, J. Nucl. Mater. **337–339**, 186 (2005).
[16] S. Murakami *et al.*, Trans. Fusion Technol. **27**, 256 (1995).
[17] H. Yamada, R. Sakamoto *et al.*, Fusion Eng. Des. **49-50**, 915-920 (2000).
[18] H. Takenaga, K. Tanaka, K. Muraoka *et al.*, Nucl. Fusion **48**, 075004 (2008).
[19] K. Tanaka, C. Michael, H. Takenaga, K. Muraoka *et al.*, "Particle transport and fluctuation characteristics around the neoclassically optimized configuration in LHD," submitted to Plasma Fusion Res.
[20] C. Angioni *et al.*, Phys. Plasmas **10**, 3225 (2003).
[21] O. Yamagishi *et al.*, Phys. Plasmas **14**, 012505 (2007).
[22] K. Tanaka *et al.*, Rev. Sci. Instrum. **77**, 10E912 (2006).
[23] J. Wesson, *Tokamaks third edition* (Clarendom Press, 2004).
[24] T.H. Watanabe *et al.*, Nucl. Fusion **47**, 1383 (2007).
[25] K. Tanaka *et al.*, Plasma Phys. Control. Fusion **44**, A231 (2002).
[26] K. Yamazaki, J. Plasma Fusion Res. **79**, 739 (2003).
[27] T. Akiyama, K. Tanaka, L.N. Vyacheslavov, A. Sanin, T. Tokuzawa, Y. Ito, S. Tsuji-Iio, S. Okajima and K. Kawahata, Rev. Sci. Instrum. **74**, 2695 (2003).
[28] K. Tanaka, L.N. Vyacheslavov, K. Kawahata, T. Tokuzawa and S. Okajima, Rev. Sci. Instrum. **75**, 3429 (2004).
[29] K. Tanaka *et al.*, Plasma Fusion Res. **2**, S1033 (2007). (http://www.jspf.or.jp/PFR/PDF/pfr2007_02-S1033.pdf)
[30] N. Ohyabu *et al.*, Phys. Rev. Lett. **97**, 055002 (2006).
[31] K. Tanaka *et al.*, J. Phys.: Conf. Ser. **123**, 012020 (2008).